

A low-rank complexity reduction algorithm for the high-dimensional kinetic chemical master equation

Lukas Einkemmer^{*†} Julian Mangott^{*} Martina Prugger[‡]

September 18, 2023

Abstract

It is increasingly realized that taking stochastic effects into account is important in order to study biological cells. However, the corresponding mathematical formulation, the chemical master equation (CME), suffers from the curse of dimensionality and thus solving it directly is not feasible for most realistic problems. In this paper we propose a dynamical low-rank algorithm for the CME that reduces the dimensionality of the problem by dividing the reaction network into partitions. Only reactions that cross partitions are subject to an approximation error (everything else is computed exactly). This approach, compared to the commonly used stochastic simulation algorithm (SSA, a Monte Carlo method), has the advantage that it is completely noise-free. This is particularly important if one is interested in resolving the tails of the probability distribution. We show that in some cases (e.g. for the lambda phage) the proposed method can drastically reduce memory consumption and run time and provide better accuracy than SSA.

1 Introduction

Chemical kinetics is an indispensable tool in order to understand reaction networks that govern, for example, the chemical processes inside a biological cell. The fundamental mathematical description of such systems is the chemical master equation (CME). However, since each chemical species adds a dimension to the CME, solving it numerically is extremely expensive. More precisely, the memory required and the computational cost scales exponentially in the number of species. This is often referred to as the *curse of dimensionality*. As a consequence, reduced models that only take averaged population numbers into account are most commonly used [10]. This assumption results in a set of ordinary differential equations (ODE) that can then be solved at low computational cost. ODE models are also called *deterministic*, owing to the fact that they only give averaged values and thus neglect both the inherent stochasticity of the system as well as the discrete nature of population numbers. It is increasingly realized, however, that both are required in order to describe many important features in biological systems [50, 27, 44, 45]. Thus computing a solution of the full chemical master equation is required in order to understand such systems.

Directly solving the chemical master equation for realistic system sizes is either very costly or prohibitive in terms of both memory and computational cost (primarily due to the curse of dimensionality). The most commonly used approach currently is the stochastic simulation algorithm (SSA; see, e.g., [25, 29]). The SSA is a Monte Carlo approach that simulates individual trajectories of the system. While one such sample, owing to the inherent randomness, does not tell us much useful information, repeating it many times allows us to collect a statistic of the most likely outcomes of the system. As a Monte Carlo method SSA does not suffer from the curse of dimensionality. However, it only converges slowly (as $1/\sqrt{N}$, where N is the number of samples) and is very noisy if not enough samples are used. The latter is a phenomenon where even if the probability density function is perfectly smooth, the algorithm approximates it by a jagged line. This, in particular, is an issue for the tail of the distribution, where the noise can completely bury the physical behavior of the system.

^{*}Department of Mathematics, Universität Innsbruck, Innsbruck, Tyrol, Austria

[†]lukas.einkemmer@uibk.ac.at

[‡]Department of Biochemistry, Universität Innsbruck, Innsbruck, Tyrol, Austria

In this paper we propose a method that directly reduces the dimensionality of the problem by using a low-rank approximation. In this approach, lower-dimensional basis functions (which require far less memory to store) are combined in order to obtain an approximation to the high-dimensional problem. For the degrees of freedom in the low-rank approximation (also called the *low-rank factors*) we derive evolution equations that are then used to advance the approximation forward in time. This dynamical low-rank approach dates back to early work in quantum mechanics (see, e.g., [42, 41, 38]) and a number of important mathematical advances in constructing and analyzing such methods have been made more recently [39, 34, 8, 6, 21, 15, 7, 13, 18]. In the quantum mechanics context usually single-orbital basis functions, which only depend on the coordinates of a single electron, are combined to obtain an approximation to the high-dimensional wave function. In [31] this idea has been directly applied to the chemical master equation. The problem with that approach, however, is that each of the low-rank factors are only allowed to depend on a single species. It is doubtful that in biological applications, given the intricate structures of complex biological networks [3], we can consider each species independently, while still obtaining an accurate approximation with a small rank.

What we propose in this paper is to divide a reaction network into two partitions. The low-rank factors are then allowed to depend on all species in their respective partition. Thus, all reactions inside of a partition are treated exactly. An approximation is only performed if a reaction crosses the partition boundary. This allows us to keep species that tightly couple to each other together without introducing any error, while still taking advantage of the computational and memory savings of the dynamical low-rank approach. We emphasize that computational savings are not only due to lower-dimensional low-rank factors, but also depend crucially on how small the rank (i.e. the number of such low-rank factors used) can be chosen while still maintaining accurate results. A similar approach has been used in [48] for Boolean models in biology. In the present work we extend this to the full kinetic chemical master equation. Let us also note that similar approaches have been used for problems in plasma physics (see, e.g., [19, 5, 12, 20]) and radiation transport (see, e.g., [47, 46, 35, 16, 17, 36]). In this case the partitioning is also based on the underlying physical problem (either a decomposition into spatial and velocity scales, as in [47, 35, 20, 19], or in coordinates parallel and perpendicular to the magnetic field, as in [14]). Our view is that in biological applications there are a multitude of different reaction networks and, in general, for each a different partitioning will give optimal results.

The remainder of the paper is structured as follows. In section 2 we introduce the chemical master equation and set our notation. The dynamical low-rank approximation is then described in detail in section 3. In section 4 we discuss the steps that are necessary in order to obtain an efficient implementation. In section 5 we investigate the accuracy and efficiency of the method for a number of examples. In particular, we show that for a lambda phage model the proposed algorithm is more accurate than SSA and drastically reduces the required run time. Finally, we conclude in section 6.

2 Chemical master equation

A well-stirred chemical reaction system of N species S_1, \dots, S_N is interacting through M reaction channels R_1, \dots, R_M . In the stochastic description the system is represented by a random variable $\mathcal{X}(t) = (\mathcal{X}_1(t), \dots, \mathcal{X}_N(t))$ on the discrete state space \mathbb{N}_0^N , where the entries $\mathcal{X}_i(t)$ denote the population number (i.e. number of molecules) of the i -th species at time t . The probability density

$$P(t, x) = \mathbb{P}(\mathcal{X}_1(t) = x_1, \dots, \mathcal{X}_N(t) = x_N), \quad x = (x_1, \dots, x_N) \in \mathbb{N}_0^N,$$

where x are the population numbers, is the solution of the kinetic chemical master equation (CME)

$$\partial_t P(t, x) = \sum_{\mu=1}^M (a_\mu(x - \nu_\mu) P(t, x - \nu_\mu) - a_\mu(x) P(t, x)). \quad (1)$$

By defining the linear operator

$$(\mathcal{A}P(t, \cdot))(x) = \sum_{\mu=1}^M (a_\mu(x - \nu_\mu) P(t, x - \nu_\mu) - a_\mu(x) P(t, x)), \quad (2)$$

the CME can be concisely written as

$$\partial_t P(t, \cdot) = \mathcal{A}P(t, \cdot).$$

The stoichiometric vector $\nu_\mu = (\nu_{\mu,1}, \dots, \nu_{\mu,N}) \in \mathbb{Z}^N$ describes the population change caused by reaction μ . The propensity function $a_\mu(x) : \mathbb{N}_0^N \rightarrow [0, \infty)$ for reaction channel R_μ can be interpreted as a transition probability $T_\mu(x + \nu_\mu | x)$. Note that the arguments $x - \nu_\mu$ in the first term of the right-hand side of equation (1) have to be omitted when they become negative (there can be no physical reaction that reduces the population number to negative values). The term “kinetic” indicates that the population number can be of any natural number (including 0), in contrast to models that treat only boolean states (where a species can be either “activated” or “not activated”; see, e.g., [11, 52, 51, 48]). For more details on the CME in general, we refer the reader to, e.g., [25, 26, 22].

We will illustrate these concepts with a simple example. The bimolecular reaction $A + B \rightleftharpoons C$ has propensity functions $a_f(x)$ for the forward and $a_b(x)$ for the backward reaction, with $x = (x_A, x_B, x_C)$. The propensity functions describe how likely the associated reaction occurs for the given population number. In the forward reaction a particle of species A reacts with a particle of species B and yields one of species C , so $\nu_f = (-1, -1, 1)$. Similarly, the stoichiometric vector for the backward reaction is $\nu_b = (1, 1, -1)$. The entire CME therefore reads as

$$\partial_t P(t, x) = a_f(x - \nu_f)P(t, x - \nu_f) + a_b(x - \nu_b)P(t, x - \nu_b) - (a_f(x) + a_b(x))P(t, x).$$

An important physical relation is the conservation of probability (also called *conservation of mass*),

$$\sum_{x \in \mathbb{N}_0^N} P(t, x) = \sum_{x \in \mathbb{N}_0^N} P(0, x) = 1, \quad (3)$$

which can be directly derived from the CME. To see this, we integrate equation (1) over time and perform a summation over x , yielding

$$\sum_{x \in \mathbb{N}_0^N} (P(t, x) - P(0, x)) = \int_0^t \sum_{\mu=1}^M \sum_{x \in \mathbb{N}_0^N} (a_\mu(x - \nu_\mu)P(\tilde{t}, x - \nu_\mu) - a_\mu(x)P(\tilde{t}, x)) d\tilde{t}. \quad (4)$$

The right-hand-side of this equation vanishes since

$$\sum_{\mu=1}^M \sum_{x \in \mathbb{N}_0^N} a_\mu(x - \nu_\mu)P(t, x - \nu_\mu) = \sum_{\mu=1}^M \sum_{x \in \mathbb{N}_0^N} a_\mu(x)P(t, x), \quad (5)$$

which implies the desired result.

3 Dynamical low-rank approximation

Solving the full CME is not possible in most cases due to the curse of dimensionality. Even the memory requirement for storing the full probability density function with a finite number \tilde{n} of possible population numbers for the N species scales with $\mathcal{O}(\tilde{n}^N)$. Therefore, we have to reduce the system size in order to solve the CME using currently available hardware. We will do this using a dynamical low-rank approximation. The main idea is to split the species (and thus the reaction network) into two partitions. Reaction pathways lying within a partition are treated exactly, while reaction pathways that cross the two partitions are taken into account in an approximate way.

More specifically, we separate the reaction network into two partitions, such that there are $m_1 < N$ species lying in partition 1. We write the population numbers as $x = (x_{(1)}, x_{(2)})$, such that $x_{(1)} = (x_1, \dots, x_{m_1})$ and $x_{(2)} = (x_{m_1+1}, \dots, x_N)$ are the population numbers in partition 1 and 2, respectively. In the following, we will denote all tuples belonging to the first or second partition by parenthesized indices, i.e. by (1) or (2). Then the CME reads as

$$\begin{aligned} \partial_t P(t, x_{(1)}, x_{(2)}) &= \sum_{\mu=1}^M a_\mu(x_{(1)} - \nu_{\mu,(1)}, x_{(2)} - \nu_{\mu,(2)})P(t, x_{(1)} - \nu_{\mu,(1)}, x_{(2)} - \nu_{\mu,(2)}) \\ &\quad - \sum_{\mu=1}^M a_\mu(x_{(1)}, x_{(2)})P(t, x_{(1)}, x_{(2)}). \end{aligned} \quad (6)$$

The dynamical low-rank (DLR) approximation of P is given by

$$P(t, x_{(1)}, x_{(2)}) \approx \sum_{i,j=1}^r X_i^1(t, x_{(1)}) S_{ij}(t) X_j^2(t, x_{(2)}), \quad (7)$$

where $S_{ij} \in \mathbb{R}$ is the coefficient matrix and r is called the *rank of the representation*. The dependency of P on $x_{(1)}$ and $x_{(2)}$ is approximated by the basis functions $\{X_i^1 : i = 1, \dots, r\}$ and $\{X_j^2 : j = 1, \dots, r\}$. These functions depend on time t but only on the population numbers in partition 1, $x_{(1)} \in \mathbb{N}_0^{m_1}$ or on the population numbers in partition 2, $x_{(2)} \in \mathbb{N}_0^{m_2}$ (with $m_2 = N - m_1$). The crucial benefit of this approach is that the memory requirements for storing the low-rank factors $X_i^1(t, x_{(1)})$, $S_{ij}(t)$ and $X_j^2(t, x_{(2)})$ scales with $\mathcal{O}((\tilde{n}^{m_1} + \tilde{n}^{m_2}) \cdot r + r^2)$. As r is usually small, the memory requirements are reduced drastically compared to the full probability density, which would require $\mathcal{O}(\tilde{n}^{m_1+m_2})$. In the following we will add additional constraints so as to obtain uniqueness of the representation given by equation (7) and derive an algorithm for computing $X_i^1(t, x_{(1)})$, $S_{ij}(t)$ and $X_j^2(t, x_{(2)})$.

Let us assume that S is invertible and X_i^1 and X_i^2 obey the orthogonality and gauge conditions

$$\langle X_i^1, X_j^1 \rangle_1 = \delta_{ij} \quad \text{and} \quad \langle X_i^2, X_j^2 \rangle_2 = \delta_{ij}, \quad (\text{orthogonality}), \quad (8)$$

$$\langle X_i^1, \partial_t X_j^1 \rangle_2 = 0 \quad \text{and} \quad \langle X_i^1, \partial_t X_j^1 \rangle_2 = 0, \quad (\text{gauge condition}), \quad (9)$$

where δ_{ij} denotes the Kronecker delta and $\langle \cdot, \cdot \rangle_k$ the inner product on $\ell^2(\mathbb{N}_0^{m_k})$ ($k = 1, 2$). Then the approximation $P \in \ell^2(\mathbb{N}_0^N)$ is unique (see, e.g., [32, 19]) and lies for any time t in the low-rank manifold

$$\mathcal{M} = \left\{ P \in \ell^2(\mathbb{N}_0^N) : P(x_{(1)}, x_{(2)}) = \sum_{i,j=1}^r X_i^1(x_{(1)}) S_{ij} X_j^2(x_{(2)}), \right. \\ \left. \text{with invertible } S = S_{ij} \in \mathbb{R}^{r \times r}, X_i^k \in \ell^2(\mathbb{N}_0^{m_k}) \text{ and } \langle X_i^k, X_j^k \rangle_k = \delta_{ij} \ (k = 1, 2) \right\}$$

with tangent space

$$\mathcal{T}_P \mathcal{M} = \left\{ \dot{P} \in \ell^2(\mathbb{N}_0^N) : \dot{P}(x_{(1)}, x_{(2)}) = \sum_{i,j=1}^r \left(\dot{X}_i^1(x_{(1)}) S_{ij} X_j^2(x_{(2)}) + X_i^1(x_{(1)}) \dot{S}_{ij} X_j^2(x_{(2)}) + X_i^1(x_{(1)}) S_{ij} \dot{X}_j^2(x_{(2)}) \right), \right. \\ \left. \text{with } \dot{S} \in \mathbb{R}^{r \times r}, \dot{X}_i^k \in \ell^2(\mathbb{N}_0^{m_k}) \text{ and } \langle X_i^k, \dot{X}_j^k \rangle_k = 0 \ (k = 1, 2) \right\},$$

where dotted quantities denote the formal derivative with respect to time. Using the orthogonality (8), the gauge conditions (9) and the linear operator defined in equation (2), we then obtain the following relations

$$\partial_t S_{ij} = \left\langle X_i^1 X_j^2, \mathcal{A} \sum_{i,j=1}^r X_i^1 S_{ij} X_j^2 \right\rangle_{1,2}, \\ \sum_{j=1}^r S_{ij} \partial_t X_j^2 = \left\langle X_i^1, \mathcal{A} \sum_{i,j=1}^r X_i^1 S_{ij} X_j^2 \right\rangle_1 - \sum_{j=1}^r \partial_t S_{ij} X_j^2, \\ \sum_{i=1}^r S_{ij} \partial_t X_i^1 = \left\langle X_j^2, \mathcal{A} \sum_{i,j=1}^r X_i^1 S_{ij} X_j^2 \right\rangle_2 - \sum_{i=1}^r X_i^1 \partial_t S_{ij}. \quad (10)$$

In principle we can solve this set of equations and thus we can determine the time evolution of the low-rank factors. However, if, e.g. a classic Runge–Kutta method is applied to equation (10), we need to invert S . If S has small singular values, inverting it is numerically very ill-conditioned. If, on the other hand, S has only large singular values, then the approximation is very inaccurate (this corresponds to the case where the rank r has been chosen too small to obtain an accurate approximation). This has been realized early in the development of such schemes, with regularization being a somewhat unsatisfactory remedy (see, e.g., [38, 41]). In the seminal paper [39] a projector splitting scheme was introduced that avoids the

inversion of S and thus results in a method that is robust with respect to the presence of small singular values. Later the basis updating Galerkin (BUG, also called the unconventional integrator) approach was introduced in [7] and improved in [6]. Any of these robust integrators would be suitable for the task at hand. However, since [48] (for the Boolean case) and [14] (for a kinetic problem from plasma physics) seems to indicate that for reversible problems the projector splitting integrator seems to be more accurate, consumes less memory and incurs less computational cost, we will mostly focus on this approach here. Let us, however, duly note that the integrators are very similar in the sense that the building blocks we derive below can also be used easily to implement any of the variants of the BUG integrator.

We can write equation (10) as

$$\partial_t P = \mathcal{P}(P) \mathcal{A} \sum_{i,j=1}^r X_i^1 S_{ij} X_j^2, \quad (11)$$

where P is given by the low-rank approximation in equation (7) and $\mathcal{P}(P)$ is the projector onto the tangent space $\mathcal{T}_P \mathcal{M}$

$$\mathcal{P}(P)g = \sum_{j=1}^r \langle X_j^2, g \rangle_2 X_j^2 - \sum_{i,j=1}^r X_i^1 \langle X_i^1 X_j^2, g \rangle_{1,2} X_j^2 + \sum_{i=1}^r X_i^1 \langle X_i^1, g \rangle_1,$$

for more details see, e.g., [39, 19]. The idea of the projector splitting integrator is to treat each term in the projector separately. That is, we split equation (11) into the following three parts

$$\partial_t P = \sum_{j=1}^r \left\langle X_j^2, \mathcal{A} \sum_{i,j=1}^r X_i^1 S_{ij} X_j^2 \right\rangle_2 X_j^2, \quad (12)$$

$$\partial_t P = - \sum_{i,j=1}^r X_i^1 \left\langle X_i^1 X_j^2, \mathcal{A} \sum_{i,j=1}^r X_i^1 S_{ij} X_j^2 \right\rangle_{1,2} X_j^2, \quad (13)$$

$$\partial_t P = \sum_{i=1}^r X_i^1 \left\langle X_i^1, \mathcal{A} \sum_{i,j=1}^r X_i^1 S_{ij} X_j^2 \right\rangle_1. \quad (14)$$

We will now explain the algorithm for computing $X_i^1(t, x_{(1)})$, $S_{ij}(t)$ and $X_j^2(t, x_{(2)})$ by using the first-order Lie-Trotter splitting. The initial value for the algorithm is given by

$$P(0, x_{(1)}, x_{(2)}) = \sum_{i,j=1}^r X_{0,i}^1(x_{(1)}) S_{0,ij} X_{0,j}^2(x_{(2)}).$$

In the first step of the algorithm, we solve equation (12). We write

$$P(t, x_{(1)}, x_{(2)}) = \sum_{j=1}^r K_j(t, x_{(1)}) X_j^2(t, x_{(2)}), \quad \text{with} \quad K_j(t, x_{(1)}) = \sum_{i=1}^r X_i^1(t, x_{(1)}) S_{ij}(t),$$

this step is therefore commonly called the *K step*. Inserting this expression into equation (12) yields an equation whose solution is given by the *time-independent* functions $X_j^2(t, x_{(2)}) = X_j^2(0, x_{(2)}) = X_{0,j}^2(x_{(2)})$ (see, e.g., [19, 39]). After applying an inner product $\langle X_i^2(x_{(2)}), \cdot \rangle_2$ and using the orthogonality condition (8), we further obtain

$$\partial_t K_i(t, x_{(1)}) = \sum_{\mu=1}^M \sum_{j=1}^r \left(c_{ij}^{1;\mu}(x_{(1)}) K_j(t, x_{(1)} - \nu_{\mu,(1)}) - d_{ij}^{1;\mu}(x_{(1)}) K_j(t, x_{(1)}) \right), \quad (15)$$

with the *time-independent* coefficients

$$\begin{aligned} c_{ij}^{1;\mu}(x_{(1)}) &= \langle X_{0,i}^2(x_{(2)}), a_{\mu}(x_{(1)} - \nu_{\mu,(1)}, x_{(2)} - \nu_{\mu,(2)}) X_{0,j}^2(x_{(2)} - \nu_{\mu,(2)}) \rangle_2, \\ d_{ij}^{1;\mu}(x_{(1)}) &= \langle X_{0,i}^2(x_{(2)}), a_{\mu}(x_{(1)}, x_{(2)}) X_{0,j}^2(x_{(2)}) \rangle_2. \end{aligned} \quad (16)$$

The coefficients can be simplified when the propensity function $a_\mu(x_{(1)}, x_{(2)})$ factorizes in its arguments or depends only on a subset of the population numbers, as we will investigate later. We now integrate equation (15) with the initial value

$$K_j(0, x_{(1)}) = \sum_{i=1}^r X_{0,i}^1(x_{(1)}) S_{0,ij}$$

until time τ to obtain $K_{1,j}(x_{(1)}) = K_j(\tau, x_{(1)})$. Then, we perform a QR decomposition

$$K_{1,j}(x_{(1)}) = \sum_{i=1}^r X_{1,i}^1(x_{(1)}) \hat{S}_{ij},$$

which gives orthonormal functions $X_{1,i}^1$ (remember that on the low-rank manifold the orthogonality condition (8) has to be fulfilled) and the matrix \hat{S}_{ij} .

In the second step of the algorithm we proceed in a similar way for equation (13) and notice that the solution is given by time-independent functions $X_i^1(t, x_{(1)}) = X_i^1(\tau, x_{(1)}) = X_{1,i}^1(x_{(1)})$ and $X_j^2(t, x_{(2)}) = X_j^2(0, x_{(2)}) = X_{0,j}^2(x_{(2)})$. After a similar calculation as for the K step, we obtain the central equation for the S step

$$\partial_t S_{ij}(t) = - \sum_{k,l=1}^r S_{kl}(t) (e_{ijkl} - f_{ijkl}), \quad (17)$$

with the time-independent coefficients

$$\begin{aligned} e_{ijkl} &= \sum_{\mu=1}^M \langle X_{1,i}^1(x_{(1)}) X_{0,j}^2(x_{(2)}), a_\mu(x_{(1)} - \nu_{\mu,(1)}, x_{(2)} - \nu_{\mu,(2)}) X_{1,k}^1(x_{(1)} - \nu_{\mu,(1)}) X_{0,l}^2(x_{(2)} - \nu_{\mu,(2)}) \rangle_{1,2}, \\ f_{ijkl} &= \sum_{\mu=1}^M \langle X_{1,i}^1(x_{(1)}) X_{0,j}^2(x_{(2)}), a_\mu(x_{(1)}, x_{(2)}) X_{1,k}^1(x_{(1)}) X_{0,l}^2(x_{(2)}) \rangle_{1,2}. \end{aligned} \quad (18)$$

Note the minus sign in front of the right-hand side of equation (17), which amounts to an integration backwards in time. Integrating equation (17) with the initial value $S_{ij}(0) = \hat{S}_{ij}$ until time τ yields $\tilde{S}_{ij} = S_{ij}(\tau)$.

In the third and last step, we set

$$P(t, x_{(1)}, x_{(2)}) = \sum_{i=1}^r X_i^1(t, x_{(1)}) L_i(t, x_{(2)}), \quad \text{with} \quad L_i(t, x_{(2)}) = \sum_{j=1}^r S_{ij}(t) X_j^2(t, x_{(2)})$$

and use this representation for equation (14). Now X_i^1 remains constant and a similar calculation as for the two previous steps yields the equation for the L step

$$\partial_t L_i(t, x_{(2)}) = \sum_{\mu=1}^M \sum_{j=1}^r \left(c_{ij}^{2,\mu}(x_{(2)}) L_j(t, x_{(2)} - \nu_{\mu,(2)}) - d_{ij}^{2,\mu}(x_{(2)}) L_j(t, x_{(2)}) \right) \quad (19)$$

with the time-independent coefficients

$$\begin{aligned} c_{ij}^{2,\mu}(x_{(2)}) &= \langle X_{1,i}^1(x_{(1)}), a_\mu(x_{(1)} - \nu_{\mu,(1)}, x_{(2)} - \nu_{\mu,(2)}) X_{1,j}^1(x_{(1)} - \nu_{\mu,(1)}) \rangle_2, \\ d_{ij}^{2,\mu}(x_{(2)}) &= \langle X_{1,i}^1(x_{(1)}), a_\mu(x_{(1)}, x_{(2)}) X_{1,j}^1(x_{(1)}) \rangle_2. \end{aligned} \quad (20)$$

We integrate equation (19) with the initial value

$$L_i(0, x_{(2)}) = \sum_{j=1}^r \tilde{S}_{ij} X_{0,j}^2(x_{(2)})$$

until time τ to obtain $L_{1,j}(x_{(2)}) = L_j(\tau, x_{(2)})$. Performing a QR decomposition

$$L_{1,i}(x_{(2)}) = \sum_{j=1}^r S_{1,ij} X_{1,j}^2(x_{(2)})$$

yields the orthonormal functions $X_{1,j}^2$ and the matrix $S_{1,ij}$, which completes the first-order Lie-Trotter projector splitting algorithm. The approximation to the solution at time τ is then given by

$$P(\tau, x) \approx \sum_{i,j=1}^r X_{1,i}^1(x_{(1)}) S_{1,ij}(t) X_{1,j}^2(x_{(2)}).$$

We note that this approach can be easily extended to, e.g., the second-order Strang splitting (see, e.g., [19, 14]).

4 Algorithm and implementation

The CME can be regarded as an infinite system of ordinary differential equations (ODEs) or as a discrete partial differential equation (PDE) with spatial differences instead of derivatives [31]. In order to turn the CME into a finite problem, we truncate the state space to a finite domain which allows a numerical solution and still captures enough of the information of the full (infinite) system. If we define the truncated state space as $\Omega^{\zeta,\eta} = \{x \in \mathbb{N}_0^N : \zeta_i \leq x_i \leq \eta_i \text{ for } i = 1, \dots, N\}$, where $\zeta_i \in \mathbb{N}_0$ and $\eta_i \in \mathbb{N}_0$ and $\zeta_i < \eta_i$ ($i = 1, \dots, N$), then the truncation error can be estimated as follows:

We denote by $\mathcal{A}^{\zeta,\eta}$ the restriction of the linear operator \mathcal{A} (defined in equation 2) to $\Omega^{\zeta,\eta}$ and by $P^{\zeta,\eta}(t)$ the solution of the restricted CME $\partial_t P^{\zeta,\eta}(t) = \mathcal{A}^{\zeta,\eta} P^{\zeta,\eta}(t)$ with initial condition $P^{\zeta,\eta}(0)$, which is the initial probability distribution restricted to the truncated state space. Defining the total mass $m^{\zeta,\eta} = \sum_{x \in \Omega^{\zeta,\eta}} P^{\zeta,\eta}(t, x)$ and assuming that $m^{\zeta,\eta} \geq 1 - \epsilon$, [43] showed that

$$P(t, x) - \epsilon \leq P^{\zeta,\eta}(t, x) \leq P(t, x) \quad \text{for } x \in \Omega^{\zeta,\eta}.$$

These inequalities give an estimation of how close the truncated state space solution approximates the true solution. The main issue of the truncation is how to determine suitable ζ and η for given final time t and tolerance $\epsilon > 0$, such that $m^{\zeta,\eta} \geq 1 - \epsilon$. Solving the reaction network deterministically with ODEs (which is cheap) or biological insight into the system might give a good idea on how to choose ζ and η a priori. Alternatively, one can implement a scheme with an adaptive truncated state space where the error in mass is used as an indicator.

In our numerical implementation we work with truncated state spaces $\Omega_1^{\zeta,\eta} = \{x_{(1)} \in \mathbb{N}_0^{m_1} : \zeta_i \leq x_i \leq \eta_i \text{ for } i = 1, \dots, m_1\}$ and $\Omega_2^{\zeta,\eta} = \{x_{(2)} \in \mathbb{N}_0^{m_2} : \zeta_i \leq x_i \leq \eta_i \text{ for } i = m_1 + 1, \dots, N\}$ for the two partitions of the reaction network, where ζ_i and η_i are fixed. We denote the number of degrees of freedom by $n_1 = (\zeta_1 - \eta_1 + 1) \cdot \dots \cdot (\zeta_{m_1} - \eta_{m_1} + 1)$ and $n_2 = (\zeta_{m_1+1} - \eta_{m_1+1} + 1) \cdot \dots \cdot (\zeta_N - \eta_N + 1)$ for partition 1 and 2, respectively. The total number of degrees of freedom is $n = n_1 n_2$.

In the implementation we will store quantities depending on the population number (such as $X_i^1(x_{(1)})$ and $X_j^2(x_{(2)})$) as matrices. As $x_{(1)}$ and $x_{(2)}$ are vectors of size m_1 and m_2 , respectively, we have to linearize the population number dependency in order to store for example $X_i^1(x_{(1)})$ and $X_j^2(x_{(2)})$ as matrices. We achieve this by introducing bijective maps $\alpha : \Omega_1^{\zeta,\eta} \rightarrow \{1, \dots, n_1\}$ and $\beta : \Omega_2^{\zeta,\eta} \rightarrow \{1, \dots, n_2\}$ and thus construct matrices $X^1 = (\underline{X}_1^1, \dots, \underline{X}_r^1) \in \mathbb{R}^{n_1 \times r}$ and $X^2 = (\underline{X}_1^2, \dots, \underline{X}_r^2) \in \mathbb{R}^{n_2 \times r}$, whose columns are the low-rank factors evaluated on the truncated state spaces $\Omega_1^{\zeta,\eta}$ and $\Omega_2^{\zeta,\eta}$. Note that we indicate linearized quantities by underlining them, i.e. $\underline{X}_i^1 = (X_{i,\alpha_1}^1, \dots, X_{i,\alpha_{n_1}}^1)^T$, where $\underline{\alpha} = (\alpha(x))_{x \in \Omega_1^{\zeta,\eta}}$. The matrices $K \in \mathbb{R}^{n_1 \times r}$ and $L \in \mathbb{R}^{n_2 \times r}$ are then computed by matrix multiplication, $K = X^1 S$ and $L = X^2 S^T$.

Using the substitution (5), the coefficients (16) can be written as

$$\begin{aligned} C^{1,\mu}(x_{(1)}) &= [\mathcal{T}_{2,\mu}^{-1}[X_0^2]]^T \text{diag}(a_\mu(x_{(1)})) X_0^2, \\ D^{1,\mu}(x_{(1)}) &= (X_0^2)^T \text{diag}(a_\mu(x_{(1)})) X_0^2, \end{aligned} \tag{21}$$

with $X_0^2 = X^2(t=0) \in \mathbb{R}^{n_2 \times r}$ and $C^{1,\mu}(x_{(1)}), D^{1,\mu}(x_{(1)}) \in \mathbb{R}^{r \times r}$. The *shift operator* $\mathcal{T}_{2,\mu} = \mathcal{T}_{2,\mu}^{+1}$ and the *inverse shift operator* $\mathcal{T}_{2,\mu}^{-1}$ act element-wise and are defined as

$$\mathcal{T}_{2,\mu}^{\pm 1}[X_{\underline{\beta}_i}^2] = \begin{cases} 0 & \text{if } \exists x_j = \left(\beta^{-1}(\underline{\beta}_i)\right)_j : (x_j \pm \nu_{\mu,j}^{(2)} < \zeta_j^{(2)}) \vee (x_j \pm \nu_{\mu,j}^{(2)} > \eta_j^{(2)}), j = 1, \dots, m_2 \\ X_{\underline{\beta}_i \pm \beta(\nu_{\mu}^{(2)})}^2 & \text{otherwise,} \end{cases}$$

and $\zeta = (\zeta^{(1)}, \zeta^{(2)})$ and $\eta = (\eta^{(1)}, \eta^{(2)})$. This definition approximates all terms $X^2(x_{(2)} - \nu_{\mu, (2)})$ which lie outside the truncated state space by 0, which assumes that the probability function and the low rank factors have to decay sufficiently fast within the truncated state space.

Writing $\underline{C}^{1,\mu} = (C_{\alpha_1}^{1,\mu}, \dots, C_{\alpha_{n_1}}^{1,\mu})$, the evolution equation of the K step becomes

$$\partial_t K = \left(\sum_{\mu=1}^M \mathcal{T}_{1,\mu} [\underline{K} \odot (\underline{C}^{1,\mu})^T] + \underline{K} \odot (\underline{D}^{1,\mu})^T \right), \quad (22)$$

with element-wise matrix-vector multiplication $\underline{K} \odot (\underline{D}^{1,\mu})^T = (K_{\alpha_1} (D_{\alpha_1}^{1,\mu})^T, \dots, K_{\alpha_{n_1}} (D_{\alpha_{n_1}}^{1,\mu})^T)$. The shift operator $\mathcal{T}_{1,\mu}$ is defined in a similar way as $\mathcal{T}_{2,\mu}$.

If we perform the integration over partition 2 in equations (18) first, we can reuse the coefficients $C^{1,\mu}$ and $D^{1,\mu}$ for the calculation of the S step coefficients

$$\begin{aligned} E_{ijkl} &= \sum_{\mu=1}^M (\mathcal{T}_{1,\mu}^{-1} [X_{1,i}^1])^T \text{diag} \left(\underline{C}_{jl}^{1,\mu} \right) X_{1,k}^1, \\ F_{ijkl} &= \sum_{\mu=1}^M (X_{1,i}^1)^T \text{diag} \left(\underline{D}_{jl}^{1,\mu} \right) X_{1,k}^1, \end{aligned} \quad (23)$$

with $E^\mu, F^\mu \in \mathbb{R}^{r \times r \times r \times r}$. With these coefficients we can write the evolution equation of the S step as

$$\partial_t S_{ij} = - \sum_{k,l=1}^r S_{kl} (E_{ijkl} - F_{ijkl}). \quad (24)$$

The coefficients $C^{2,\mu}, D^{2,\mu}$ are calculated via

$$\begin{aligned} C^{2,\mu}(x_{(2)}) &= [\mathcal{T}_{1,\mu}^{-1} [X_1^1]]^T \text{diag} (a_\mu(x_{(2)})) X_1^1, \\ D^{2,\mu}(x_{(2)}) &= (X_1^1)^T \text{diag} (a_\mu(x_{(2)})) X_1^1, \end{aligned} \quad (25)$$

with $X_1^1 = X^1(t = \tau) \in \mathbb{R}^{n_1 \times r}$ and $C^{2,\mu}(x_{(2)}), D^{2,\mu}(x_{(2)}) \in \mathbb{R}^{r \times r}$.

Showing a similar structure as the corresponding equation for the K step, the evolution equation for the L step reads as

$$\partial_t L = \sum_{\mu=1}^M (\mathcal{T}_{2,\mu} [\underline{L} \odot (\underline{C}^{2,\mu})^T] + \underline{L} \odot (\underline{D}^{2,\mu})^T). \quad (26)$$

Note that for the second term on the right-hand side of equation (26) we could perform the summation over all reactions R_μ before multiplying $\underline{D}^{2,\mu}$ with \underline{L} . Moreover, the calculation of the evolution equation (26) could be simplified by introducing a reaction-independent $\underline{D}^2 = \sum_{\mu=1}^M \underline{D}^{2,\mu}$. However, as we will see in section 4.1.1, it is computationally more efficient to perform the summation over all reactions after multiplying \underline{L} with the reaction-dependent $\underline{D}^{2,\mu}$. The same holds for the coefficient $\underline{D}^{1,\mu}$ and the second term on the right-hand side of the evolution equation (22) for the K step. For the first terms on the right-hand side of equations (22) and (26) we always have to keep the reaction-dependence of $\underline{C}^{1,\mu}$ and $\underline{C}^{2,\mu}$, since the shift operator is also reaction-dependent, therefore the computational effort would scale the same even when using reaction-independent D coefficients.

Finally, we want to give a remark on the computational effort for the evolution equation and the calculation of the coefficients. Without making any further simplifications, the computational effort for calculating the C and D coefficients is $\mathcal{O}(Mr^2n)$, where M was the total number of reactions channels. When we reuse $\underline{C}^{1,\mu}$ and $\underline{D}^{1,\mu}$ for the calculation of the E and F coefficients, the complexity for computing the E and F coefficients is $\mathcal{O}(Mr^4n_1)$. The right-hand side of the evolution equation for the K step requires an integration over the population numbers in partition 1, therefore the computational cost is $\mathcal{O}(Mr^2n_1)$. Similarly, the computation of the L step scales with $\mathcal{O}(Mr^2n_2)$, whereas for the S step we have complexity $\mathcal{O}(r^4)$. Note that in particular the computation of the C and D coefficients is very expensive, since it scales with the total number of degrees of freedom n . Thus it is imperative to reduce this computational burden, which is the topic of the next section.

4.1 Efficient computation of the coefficients

In the previous section we have seen that computing the coefficients without making any further assumptions is computationally expensive. The main goal here is to describe ways how to avoid the scaling of the computational effort with the total number of degrees of freedom n . We essentially discuss two possibilities to circumvent this scaling behaviour: First, most reactions only depend on a small subset of all species. When we denote for a given reaction R_μ the number of participating species (we call them *reagents*) by \tilde{N}_μ , than this assumption can be expressed as $\tilde{N}_\mu \ll N$. Second, in many reaction networks the propensity functions exhibit a so-called factorization property, and exploiting this property again reduces the computational burden. Note that our present implementation does not exploit the factorization property since in all our examples $\tilde{N}_\mu \ll N$. However, what the discussion in this section shows is that even in the rare instances where this is not the case, the factorization property which is common to most reactions gives a way forward to efficiently implementing the dynamical low-rank approach.

4.1.1 Dependence of the propensity on reagents

Since in most reactions only a subset of all species is actually participating, the propensity $a_\mu(x)$ for such a reaction R_μ only depends on the population number of the \tilde{N}_μ reagents, so $a_\mu(x) = a_\mu(\tilde{x}_\mu)$, where $\tilde{x}_\mu \in \mathbb{N}_0^{\tilde{N}_\mu}$ and $\tilde{N}_\mu \leq N$. In many cases the propensities only depend on the population number of two or three species, therefore $\tilde{N}_\mu \ll N$. The computational effort of our algorithm can be reduced substantially by calculating coefficients C and D only for the possible values of \tilde{x}_μ that are actually needed.

For a given reaction μ we first determine in the implementation the reagents and precompute all possible values of the propensity function $a_\mu(\tilde{x}_\mu)$, since those values do not change over time. The C and D coefficients have to be calculated only for \tilde{n}_1^μ or \tilde{n}_2^μ population number values, but K and L still depend on the population numbers $x_{(1)}$ and $x_{(2)}$, respectively. Therefore we have to introduce a (reaction-dependent) mapping between \tilde{x}_μ and $x_{(1)}$ in order to perform for example the multiplication $\underline{K} \odot (\underline{D}^{1,\mu})^T$ on the right-hand side in equation (22). Applying this map effectively introduces a reaction-dependency on the overall multiplication term. This is the reason why we cannot introduce the reaction independent $\underline{D}^2 = \sum_{\mu=1}^M \underline{D}^{2,\mu}$ as discussed previously.

Note that the complexity for the integration over x_1 in equation (21) still scales with $\mathcal{O}(n_1)$ and for equation (25) the integration over x_2 scales with $\mathcal{O}(n_2)$, but the coefficients have to be calculated only for the \tilde{n}_1^μ or \tilde{n}_2^μ population number values. Therefore the complexity for calculating the $\underline{C}^{1,\mu}$ and $\underline{D}^{1,\mu}$ coefficients is reduced to $\mathcal{O}(\sum_{\mu=1}^M \tilde{n}_1^\mu n_2 r^2)$, and for the $\underline{C}^{2,\mu}$ and $\underline{D}^{2,\mu}$ coefficients to $\mathcal{O}(\sum_{\mu=1}^M \tilde{n}_2^\mu n_1 r^2)$. Thus, these computations do no longer scale with n (assuming that $\tilde{N}_\mu \ll N$).

4.1.2 Factorization property of the propensity function

The equations for the coefficients (16), (18) and (20) can be simplified if the propensity function can be written as

$$a_\mu(x_{(1)}, x_{(2)}) = a_{\mu,(1)}(x_{(1)}) a_{\mu,(2)}(x_{(2)}). \quad (\text{factorization property}) \quad (27)$$

This property is valid for elementary reaction types and reactions of the Michaelis-Menten form and thus is ubiquitous in most biological systems. The factorization property enables us to rewrite for example the coefficient $c_{ij}^{1,\mu}$ in equation (16) as

$$c_{ij}^{1,\mu}(x_{(1)}) = a_{\mu,(1)}(x_{(1)} - \nu_{\mu,(1)}) \langle X_{0,i}^2(x_{(2)}), a_{\mu,(2)}(x_{(2)} - \nu_{\mu,(2)}) X_{0,j}^2(x_{(2)} - \nu_{\mu,(2)}) \rangle_2,$$

which scales with $\mathcal{O}(M r^2 (n_1 + n_2))$ compared to $\mathcal{O}(M r^2 n)$ (even when disregarding the considerations about the dependence of the propensity on reagents in the previous section). Moreover, the two inner products of the coefficient e_{ijkl} in equation (18) can be calculated independently,

$$e_{ijkl} = \sum_{\mu=1}^M \langle X_{1,i}^1(x_{(1)}) a_{\mu,(1)}(x_{(1)} - \nu_{\mu,(1)}) X_{1,k}^1(x_{(1)} - \nu_{\mu,(1)}) \rangle_1 \\ \times \langle X_{0,j}^2(x_{(2)}) a_{\mu,(2)}(x_{(2)} - \nu_{\mu,(2)}) X_{0,l}^1(x_{(2)} - \nu_{\mu,(2)}) \rangle_2,$$

which has computational costs of $\mathcal{O}(M r^4 (n_1 + n_2))$ instead of $\mathcal{O}(M r^4 n)$.

4.2 First- and second-order projector splitting integrator

The first-order integrator is obtained by using Lie–Trotter splitting as explained in section 3. The evolution equations (22) and (26) for K and L steps as well as (24) for the S step are solved with an explicit Euler method. Due to different reaction time scales stemming from both small and large propensity values, the CME becomes stiff for many systems. In order to remain in the stable region for large time step size τ , we perform k explicit Euler steps with a time step size of τ/k while keeping the coefficients constant. Note that although the computational cost for evaluating the right-hand side of the evolution equation shows the same scaling, the constant is smaller compared to the calculation of the coefficients, which however only needs to be done once or twice (for $C^{1,\mu}$ and $D^{1,\mu}$ in case of the second-order integrator) in each time step. We will explore the use of implicit integrators in future work.

The low-rank factors X^1 and X^2 and the coupling coefficients S are obtained from K and L matrices by performing a QR decomposition. In order to perform the QR decomposition and the linear algebra operations required for an efficient calculation of the coefficients we made use of the dynamical low-rank framework **Ensign** [5].

A detailed description of the first order Lie–Trotter projector splitting scheme is shown in algorithm 1.

Algorithm 1 First-order Lie–Trotter projector splitting integrator for the kinetic CME.

Input: X_0^1, S_0, X_0^2

Output: X_1^1, S_3, X_1^2

- 1: Calculate $C^{1,\mu}(x_{(1)})$ and $D^{1,\mu}(x_{(1)})$ with X_0^2 using equation (21)
 - 2: Integrate K from 0 to τ with initial value $K(0) = X_0^1 S_0$ using equation (22)
 - 3: Decompose $K(\tau) = X_1^1 S_1$ via a QR factorization
 - 4: Calculate E^μ and F^μ with $X_1^1, X_0^2, C^{1,\mu}(x_{(1)})$ and $D^{1,\mu}(x_{(1)})$ using equation (23)
 - 5: Integrate S from 0 to τ with initial value $S(0) = S_1$ using equation (24) and set $S_2 = S(\tau)$
 - 6: Calculate $C^{2,\mu}(x_{(2)})$ and $D^{2,\mu}(x_{(2)})$ with X_1^1 using equation (25)
 - 7: Integrate L from 0 to τ with initial value $L(0) = X_1^2 (S_2)^T$ using equation (26)
 - 8: Decompose $L(\tau) = X_1^2 (S_3)^T$ via a QR factorization
-

Our numerical scheme can be generalized to a second-order method by employing Strang splitting in the context of equation (11). This is shown in detail in algorithm 2. Note that two of the steps are repeated while one step is only performed once (due to the symmetry of the splitting). Ideally, the step that has to be done only once is chosen to coincide with the step that incurs the largest computational effort (either the K or the L step).

Algorithm 2 Second-order Strang projector splitting integrator for the kinetic CME.

Input: X_0^1, S_0, X_0^2

Output: X_2^1, S_5, X_1^2

- 1: Calculate $C^{1,\mu}(x_{(1)})$ and $D^{1,\mu}(x_{(1)})$ with X_0^2 using equation (21)
 - 2: Integrate K from 0 to $\tau/2$ with initial value $K(0) = X_0^1 S_0$ using equation (22)
 - 3: Decompose $K(\tau/2) = X_1^1 S_1$ via a QR factorization
 - 4: Calculate E^μ and F^μ with $X_1^1, X_0^2, C^{1,\mu}(x_{(1)})$ and $D^{1,\mu}(x_{(1)})$ using equation (23)
 - 5: Integrate S from 0 to $\tau/2$ with initial value $S(0) = S_1$ and set $S_2 = S(\tau/2)$ using equation (24)
 - 6: Calculate $C^{2,\mu}(x_{(2)})$ and $D^{2,\mu}(x_{(2)})$ with X_1^1 using equation (25)
 - 7: Integrate L from 0 to τ with initial value $L(0) = X_1^2 (S_2)^T$ using equation (26)
 - 8: Decompose $L(\tau) = X_1^2 (S_3)^T$ via a QR factorization
 - 9: Recalculate $C^{1,\mu}(x_{(1)})$ and $D^{1,\mu}(x_{(1)})$ with X_1^2 using equation (21)
 - 10: Recalculate E^μ and F^μ with X_1^1, X_1^2 and new values for $C^{1,\mu}(x_{(1)})$ and $D^{1,\mu}(x_{(1)})$ using equation (23)
 - 11: Integrate S from $\tau/2$ to τ with initial value $S(\tau/2) = S_3$ and set $S_4 = S(\tau)$ using equation (24)
 - 12: Integrate K from $\tau/2$ to τ with initial value $K(\tau/2) = X_1^1 S_4$ using equation (22)
 - 13: Decompose $K(\tau) = X_2^1 S_5$ via a QR factorization
-

5 Numerical experiments

We tested our implementation with three models from the field of biochemistry. The smallest model, the genetic toggle switch, was primarily chosen for code validation and to investigate the approximation accuracy (as a reference solution without the low-rank approximation can be computed easily). For the two larger models, the bacteriophage- λ (“lambda phage”) and the BAX pore assembly, we compare the DLR approximation with the dominating numerical method for solving the CME, the stochastic simulation algorithm (SSA) (see, e.g., [25]).

5.1 Toggle switch

The genetic toggle switch, as first described in [23], has a function analogous to a flip-flop in electronics. It consists of two mutually repressing proteins S_1 and S_2 , which leads to two stable steady-states. We studied the reaction system shown in table 1, which was also considered in [31].

No.	Reaction	Propensity function
1	$S_1 \longrightarrow \star$	$c \cdot x_1$
2	$S_2 \longrightarrow \star$	$c \cdot x_2$
3	$\star \longrightarrow S_1$	$b/(b + x_2)$
4	$\star \longrightarrow S_2$	$b/(b + x_1)$

Table 1: Reactions and propensity functions of the toggle switch systems. The two parameters are chosen as $b = 0.4$ and $c = 0.05$.

The first two reactions describe the decay of proteins S_1 and S_2 , respectively. If the population number of S_2 is large, then the propensity of reaction 3 becomes small and transcription of new copies of S_1 is inhibited. Similarly, the production of S_2 by reaction 4 is inhibited by S_1 .

As initial value we consider the Gaussian distribution

$$P(0, x) = \gamma \cdot \exp\left(-\frac{1}{2}(x - \mu)^T C^{-1}(x - \mu)\right),$$

$$C = \frac{1}{2} \begin{pmatrix} 75 & -15 \\ -15 & 75 \end{pmatrix},$$

with $\mu = (30, 5)$ and γ was determined by the condition $\sum_{x \in \Omega^{\zeta, \eta}} P(0, x) = 1$.

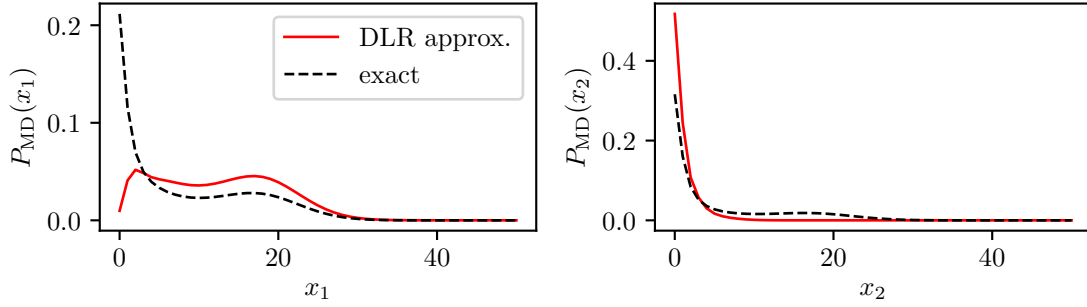
We solved the CME on the time interval $[0, 500]$ with truncation indices $\eta = (0, 0)$ and $\zeta = (50, 50)$ and with the trivial partitions $\mathcal{P}_1 = \{S_1\}$ and $\mathcal{P}_2 = \{S_2\}$. Using rank $r = 5$, the total number of degrees of freedom is reduced from $51^2 = 2601$ to $2 \cdot 51 \cdot 5 + 5^2 = 535$, which is 20.6% of the full system size. Due to the relatively small size of the truncated state space an “exact” reference solution of the full system on the truncated state space could be obtained via a Python implementation that uses the RK45 `scipy.solve_ivp` routine to directly solve equation (1).

Figure 1 shows the DLR approximation (using the second-order integrator with time step size $\tau = 0.02$ and 10 substeps) with ranks $r = 4$ and 5 and the reference solution of the one-dimensional marginal distributions $P_{\text{MD}}(x_1)$, $P_{\text{MD}}(x_2)$ at time $t = 500$. It can be clearly seen that $r = 4$ is not sufficient to capture the full behavior of the system, but for $r = 5$ we obtain very good results. Figure 2 depicts the full probability distribution $P(x_1, x_2)$ at time $t = 500$. This figure again demonstrates that the results of the DLR approximation for $r = 5$ are in very good agreement with the exact solution of the truncated CME. Using the second-order integrator with time step size $\tau = 0.02$ and 10 substeps, the total run time for the simulation with rank $r = 5$ was approximately 1 minute and 16 seconds on a MacBook Pro with a 2 GHz Intel Core i5 Skylake (6360U) processor. The results of the DLR approximation were computed with one thread.

rank $r = 4$

$$\max(|\text{DLR approx.} - \text{exact}|) = 2.02 \cdot 10^{-1}$$

$$\max(|\text{DLR approx.} - \text{exact}|) = 2.02 \cdot 10^{-1}$$



rank $r = 5$

$$\max(|\text{DLR approx.} - \text{exact}|) = 3.10 \cdot 10^{-3}$$

$$\max(|\text{DLR approx.} - \text{exact}|) = 4.60 \cdot 10^{-3}$$

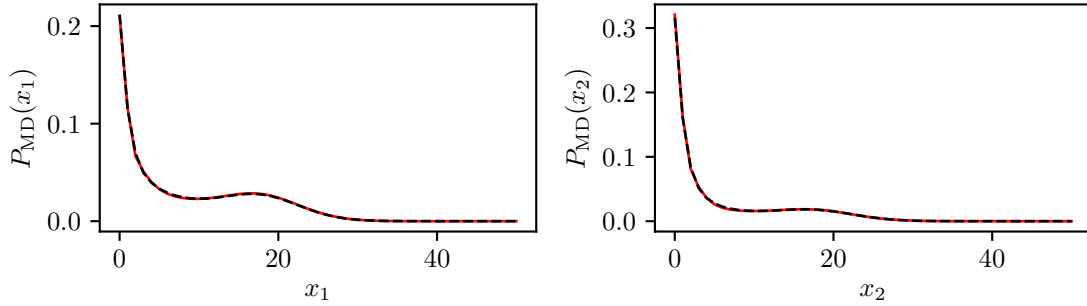


Figure 1: DLR approximation (red, solid line) and exact reference solution (black, dashed line) of the one-dimensional marginal distributions $P_{\text{MD}}(x_1)$ and $P_{\text{MD}}(x_2)$ for ranks $r = 4$ and 5 of the toggle switch example at $t = 500$. The reference solution was obtained by solving the CME directly with the `scipy.solve_ivp` routine. For the DLR approximation the second-order integrator with time step size $\tau = 0.02$ and 10 substeps were used.

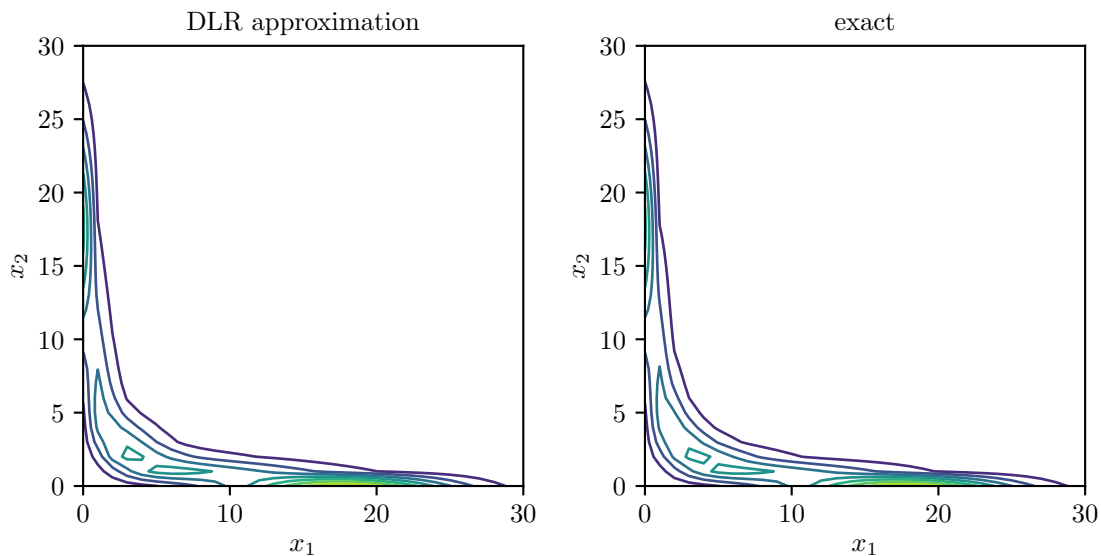


Figure 2: DLR approximation (left) and exact reference solution (right) of the full probability distribution $P(x_1, x_2)$ for the toggle switch example at $t = 500$. Note that P is only defined at the discrete grid points $x \in \mathbb{N}_0^2$; the contour plots are based on interpolation and are shown here for the sake of clarity. The reference solution was obtained by solving the CME directly with the `scipy.solve_ivp` routine. For the DLR approximation rank $r = 5$ and the second-order integrator with time step size $\tau = 0.02$ and 10 substeps were used.

Figure 3 shows the 2-norm error of the best-approximation and of the DLR approximation for time step sizes $\tau = 0.2$ and 0.02 , using the second-order integrator with 10 substeps. The best-approximation was obtained by truncating all but the first $r = 5$ singular values of a singular value decomposition (SVD) of the reference solution, for the DLR approximation we again used $r = 5$. It can be seen that using a smaller time step size helps particularly in the first few steps of the simulation. After approximately $t = 50$ the errors for the different time step sizes are almost identical, indicating that the overall error is dominated by the low-rank approximation. The error of the dynamical low-rank algorithm proposed is only slightly larger than the theoretical best approximation with the same rank.

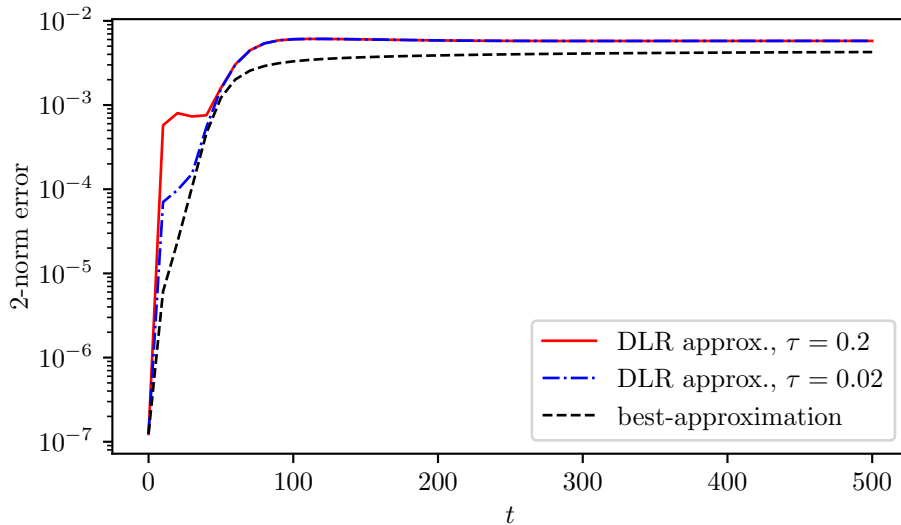


Figure 3: Comparison of the 2-norm error for the DLR approximation using time step size $\tau = 0.2$ (red, solid line) and $\tau = 0.02$ (blue, dash-dotted line) with the best-approximation (black, dashed line) as a function of time t for the toggle switch system. The error was calculated by comparing each approximation with the exact reference solution of the toggle switch. The best-approximation was obtained by truncating all but the first $r = 5$ singular values of a SVD of the reference solution. For the DLR approximation rank $r = 5$ and the second-order integrator with 10 substeps were used.

5.2 Lambda phage

As a second example, the DLR approximation was applied to the model for the life cycle of the lambda phage as described in [30]. Table 2 lists the ten reactions and five species of this system.

No.	Reaction	Propensity function
1	$\star \rightarrow S_1$	$a_1 b_1 / (b_1 + x_2)$
2	$\star \rightarrow S_2$	$(a_2 + x_5) b_2 / (b_2 + x_1)$
3	$\star \rightarrow S_3$	$a_3 b_3 x_2 / (b_3 x_2 + 1)$
4	$\star \rightarrow S_4$	$a_4 b_4 x_3 / (b_4 x_3 + 1)$
5	$\star \rightarrow S_5$	$a_5 b_5 x_3 / (b_5 x_3 + 1)$
6	$S_1 \rightarrow \star$	$c_1 \cdot x_1$
7	$S_2 \rightarrow \star$	$c_2 \cdot x_2$
8	$S_3 \rightarrow \star$	$c_3 \cdot x_3$
9	$S_4 \rightarrow \star$	$c_4 \cdot x_4$
10	$S_5 \rightarrow \star$	$c_5 \cdot x_5$

	$i = 1$	$i = 2$	$i = 3$	$i = 4$	$i = 5$
a_i	0.5	1	0.15	0.3	0.3
b_i	0.12	0.6	1	1	1
c_i	0.0025	0.0007	0.0231	0.01	0.01

Table 2: Reactions, propensity functions and parameters of the lambda phage system.

The life cycle of the lambda phage represents a naturally occurring toggle switch. The lambda phage infects *E. coli*, and depending on the environment, either stays dormant in the bacterial host (*lysogenic phase*) or multiplies, reassembles itself and breaks out of the host (*lytic phase*). If enough S_5 is present in the environment, S_2 is produced and the system is in the lysogenic phase. Abundance of S_2 in turn inhibits the formation of S_1 via reaction 1. If the amount of S_5 in the environment is scarce, the production of S_1 causes the system to enter the lytic phase and the transcription of new copies of S_2 via reaction 2 is inhibited.

As an initial value the multinomial distribution with parameters $n = 3$ and $p = (0.05, \dots, 0.05)$ has been

chosen:

$$P(0, x) = \begin{cases} \frac{3!}{x_1! \cdots x_5! (3-|x|)!} 0.05^{|x|} (1 - 5 \cdot 0.05)^{3-|x|} & \text{if } |x| \leq 3, \\ 0 & \text{else,} \end{cases}$$

where $|x| = x_1 + \cdots + x_5$. We solved the CME on the time interval $[0, 10]$ with truncation indices $\eta = (0, 0, 0, 0, 0)$ and $\zeta = (15, 40, 10, 10, 10)$. The reaction network was partitioned into $\mathcal{P}_1 = \{S_1, S_2\}$ and $\mathcal{P}_2 = \{S_3, S_4, S_5\}$, therefore the two partitions have a comparable number of degrees of freedom, $n_1 = 16 \cdot 41 = 656$ and $n_2 = 11^3 = 1331$. Using rank $r = 9$, the total number of degrees of freedom used in the DLR approximation is reduced from $n_1 \cdot n_2 = 873\,136$ to $(n_1 + n_2) \cdot r + r^2 = 17\,964$, which is 2.1% of the full system size.

An “exact” reference solution was obtained again by solving the full CME on the truncated state space with `scipy.solve_ivp`. Due to the relatively large system size the computation of the full solution is very costly and therefore substantially slower than the DLR approximation. Moreover, we compare the DLR approximation with results obtained with SSA. These latter results were computed in the systems biology framework *PySB* [37], which uses the SSA implementation *StochKit2* [49]. Table 3 gives an overview of the run times for the exact reference solution, the DLR approximation and SSA.

	run time [s]
DLR approx. ($r = 4$)	52
DLR approx. ($r = 9$)	191
SSA (10 000 runs)	855
SSA (100 000 runs)	905
SSA (1 000 000 runs)	2319
exact	1164

Table 3: Overview of the approximate run times in seconds for the DLR approximation, SSA, and the exact reference solution for the lambda phage system. The DLR approximation was computed with the second-order integrator using time step size $\tau = 0.01$ and 10 substeps. All computations were performed on a MacBook Pro with a 2 GHz Intel Core i5 Skylake (6360U) processor. The results of the DLR approximation were computed with one thread.

SSA is a Monte Carlo approach, therefore the results of this method are polluted with noise which scales only as the inverse square root of the total number of independent runs or samples. Figure 4 shows the partially evaluated probability distribution $P_S(x_2) = P(x_1 = 0, x_2, x_3 = 1, x_4 = 1, x_5 = 1)$ at time $t = 10$ computed with the DLR approximation using rank $r = 4$ and $r = 9$, as well as with SSA using 10 000, 100 000 and 1 000 000 samples. Furthermore, the exact reference solution of the CME on the truncated state space is shown for comparison. The DLR solution for $r = 4$ is in very good agreement with the reference solution, only for high population numbers $x_2 > 30$, which have a relatively low probability, a discrepancy becomes visible. For population numbers $x_2 > 36$ the results are still close to zero, but become negative and therefore are not shown in this semi-logarithmic plot. When increasing the rank to $r = 9$, the results for $x_2 > 36$ remain positive and only show a small deviation from the reference solution. The results for SSA with 10 000 runs exhibit a lot of noise and for several population numbers the probability is zero, because the corresponding state was not sampled at all during the simulation. When performing the simulation with more runs, this stochastic noise decreases, but even for 1 000 000 runs SSA has still problems to resolve the small values at the tails of the probability distribution (for example at $x_2 = 0$). This, in particular, shows that the dynamical low-rank approximation has a significant advantage if one is interested in resolving states with low probability. The reason for this is that no numerical noise is introduced by the low-rank approach. We also calculated the maximal error between the exact solution and the SSA result for $P_S(x_2)$. For 1 000 000 runs the maximal error was $7.74 \cdot 10^{-5}$ and therefore higher than for the DLR approximation for both $r = 4$ ($4.21 \cdot 10^{-5}$) and $r = 9$ ($1.03 \cdot 10^{-5}$). The computational cost of the DLR approximation, despite the lower error, is lower by a factor of approximately 45 ($r = 4$) and 12 ($r = 9$) compared to SSA with 1 000 000 samples.

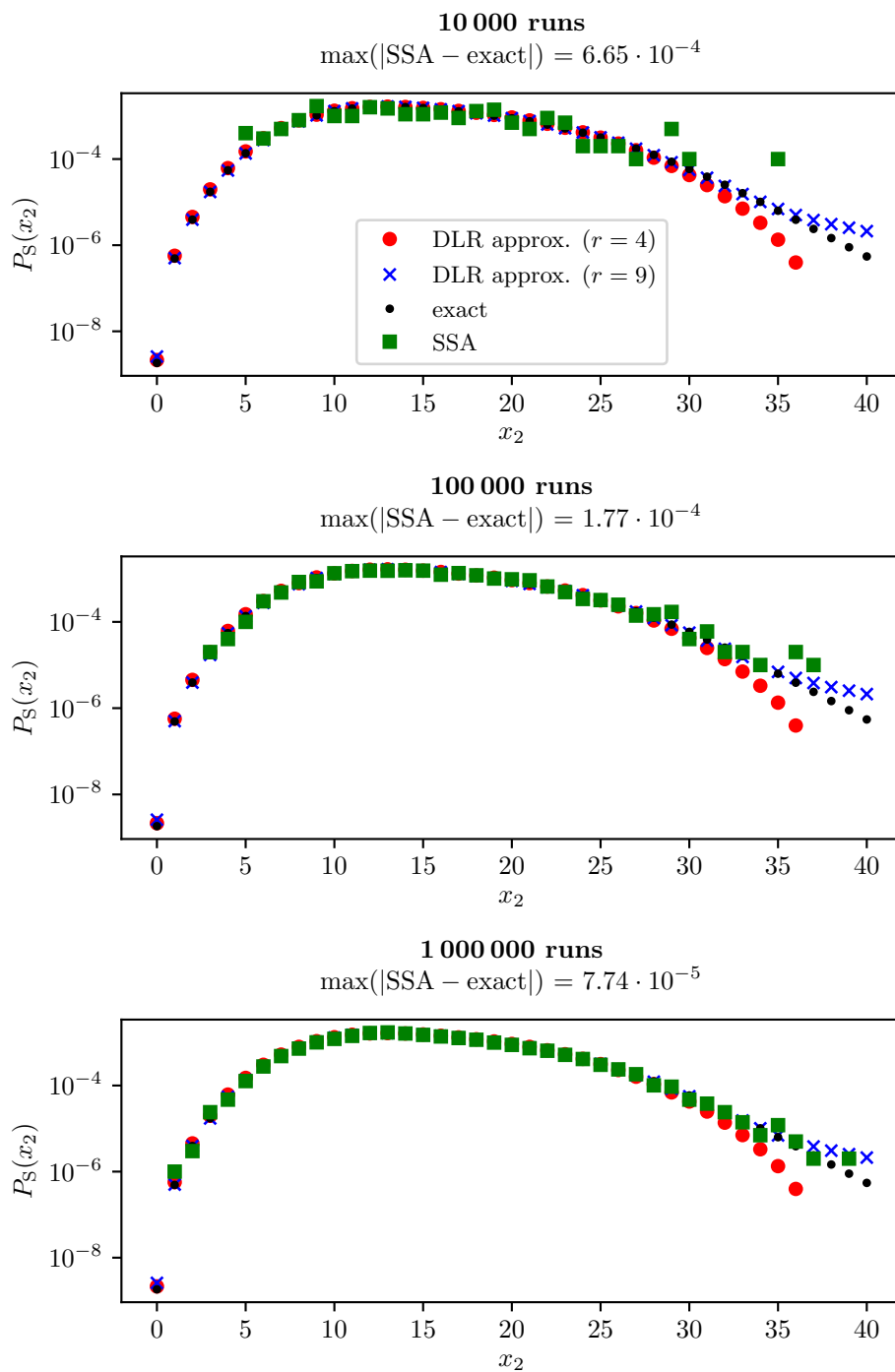


Figure 4: Partially evaluated probability distribution $P_S(x_2) = P(x_1 = 0, x_2, x_3 = 1, x_4 = 1, x_5 = 1)$ of the lambda phage system at $t = 10$. The results were obtained with our implementation of the DLR approximation using rank $r = 4$ (red dots), rank $r = 9$ (blue crosses) and with SSA (green squares) using 10 000, 100 000 and 1 000 000 samples. For comparison also the exact reference solution is shown (small black dots), which was obtained by solving the CME on the truncated state space directly with the `scipy.solve_ivp` routine. The DLR approximation was computed with the second-order integrator using time step size $\tau = 0.01$ and 10 substeps. The maximum error for the DLR approximation was $\max(|\text{DLR} - \text{exact}|) = 4.21 \cdot 10^{-5}$ for $r = 4$ and $1.03 \cdot 10^{-5}$ for $r = 9$.

The stochastic noise of SSA is also visible in figure 5. Here the partially evaluated two-dimensional probability distribution $P_S(x_1, x_2) = P(x_1, x_2, x_3 = 1, x_4 = 1, x_5 = 1)$ of the lambda phage example is shown for time $t = 10$. The probability distributions calculated with the DLR approximation for rank $r = 4$ and $r = 9$ agree very well with the exact reference solution, whereas the noise for the SSA results with 10 000 and 100 000 samples is very pronounced. Only for 1 000 000 runs the results are comparable to the ones obtained by the DLR approximation.

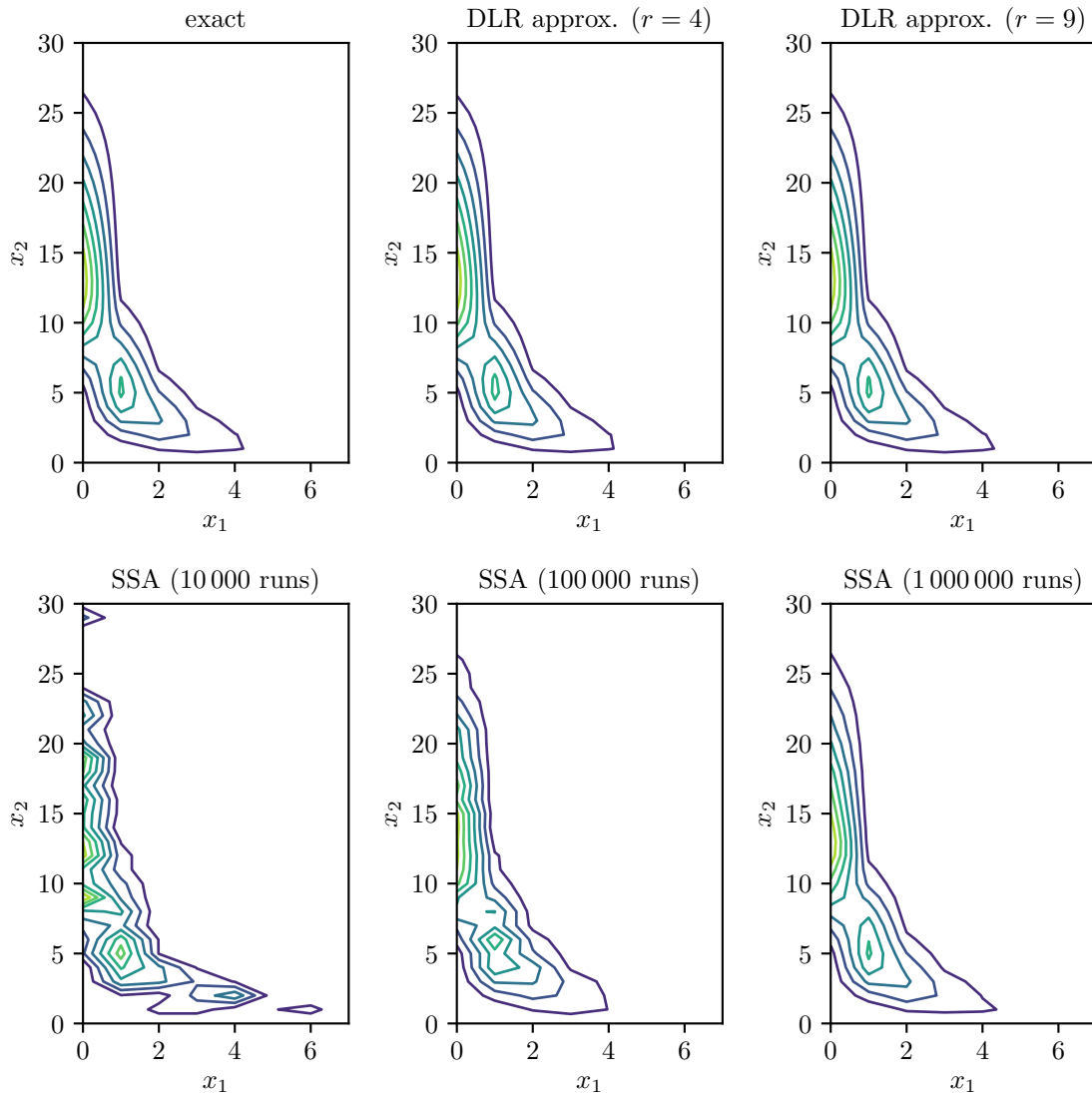


Figure 5: Partially evaluated two-dimensional probability distribution $P_S(x_1, x_2) = P(x_1, x_2, x_3 = 1, x_4 = 1, x_5 = 1)$ of the lambda phage example at $t = 10$. Top row: exact reference solution (solution of the full CME on the truncated state space with the `scipy.solve_ivp` routine) and solutions of the DLR approximation with rank $r = 4$ and $r = 9$. The DLR solutions were computed with the second-order integrator using time step size $\tau = 0.01$ and 10 substeps. Bottom row: results obtained with SSA using 10 000, 100 000 and 1 000 000 runs. Note that P_S is only defined at the discrete grid points $x \in \mathbb{N}_0^2$; the contour plots are based on interpolation and are shown here for the sake of clarity.

Figure 6 shows the 2-norm error of the probability density function for the DLR approximation, SSA and the best-approximation depending on time t . For rank $r = 4$ the resulting error of the DLR and the best-approximation is slightly larger than for the SSA using 1 000 000 samples. However, DLR in this configuration is much faster as has been noted before. If the rank is increased to $r = 9$, the DLR

approximation also significantly outperforms SSA in terms of accuracy.

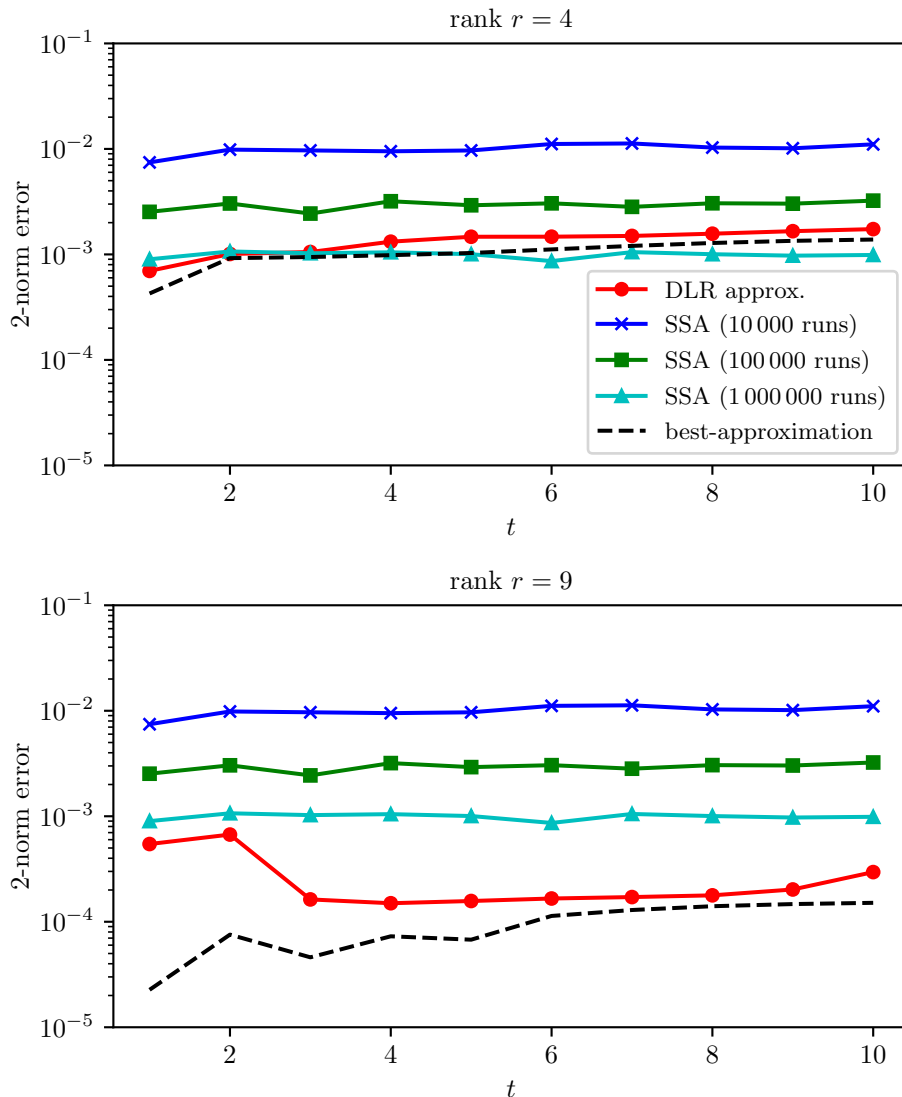


Figure 6: Comparison of the 2-norm error as a function of time t for the DLR approximation (red circles) with the best-approximation (black, dashed line) using ranks $r = 4$ (top) and $r = 9$ (bottom) and with SSA for 1000 (blue crosses), 100 000 (green squares) and 1 000 000 samples (cyan triangles) for the lambda phage example. The error was calculated by comparing each approximation with the exact reference solution of the lambda phage, which was obtained by solving the full CME on the truncated state space directly with the `scipy.solve_ivp` routine. The best-approximation was obtained by truncating all but the first $r = 4$ or $r = 9$ singular values for a SVD of the exact reference solution. For the DLR approximation the second-order integrator with time step size $\tau = 0.01$ and 10 substeps was used. Note that the 2-norm error for $t = 0$ is not shown in the plot, as it is zero up to machine precision for the best-approximation, DLR approximation and SSA with 1 000 000 runs.

5.3 BAX pore assembly

The last and most challenging example is the BAX pore assembly, which is a system with 19 reactions and 11 species. The reactions and propensity functions of this system are listed in table 4. BAX plays a key role in mediating mitochondrial outer membrane permeabilization and is therefore a regulator of

programmed cell death (*apoptosis*). The model was taken from [24] and is part of the *extrinsic apoptosis reaction model* (EARM, see, e.g., [1]). Monomeric BAX (S_1) can assemble to larger complexes (S_2 – S_5 , reactions 1–5) and the complexes in turn can dissociate (reactions 6–10). Large enough complexes are able to transport cargo (S_{10} and S_{11}), this process is described by reactions 11–19.

No.	Reaction	Propensity function
1	$S_1 + S_1 \longrightarrow S_2$	$a_f \cdot x_1(x_1 - 1)/2$
2–5	$S_i + S_1 \longrightarrow S_{i+1}$	$a_f \cdot x_i x_1$ ($i = 2, \dots, 5$)
6–10	$S_{j+1} \longrightarrow S_j + S_1$	$a_r \cdot x_{j+1}$ ($j = 1, \dots, 5$)
11–13	$S_k + S_{10} \longrightarrow S_{k+3}$	$b_f \cdot x_k x_{10}$ ($k = 4, 5, 6$)
14–16	$S_{k+3} \longrightarrow S_k + S_{10}$	$b_r \cdot x_{k+3}$
17–19	$S_{k+3} \longrightarrow S_k + S_{11}$	$c_r \cdot x_{k+3}$

Table 4: Reactions and propensity functions of the BAX pore assembly system with parameters $a_f = 2 \cdot 10^{-4}$, $a_r = b_r = 10^{-3}$, $b_f = 3 \cdot 10^{-5}$ and $c_r = 10$.

We solved the CME on the time interval $[0, 145]$ with rank $r = 5$ on the truncated state space with truncation indices $\eta = (0, 0, 0, 0, 0, 0, 0, 0, 0, 0, 0)$ and $\zeta = (46, 16, 16, 11, 11, 11, 4, 4, 4, 56, 56)$. Note that the purpose of this numerical example was to discover possible limitations of our approach; in order to reach the equilibrium one would have to consider a substantially longer interval of approximately $[0, 20\,000]$. The reaction network was partitioned into $\mathcal{P}_1 = \{S_1, S_2, S_3, S_4, S_5\}$ and $\mathcal{P}_2 = \{S_6, S_7, S_8, S_9, S_{10}, S_{11}\}$, therefore the two partitions have $n_1 = 46 \cdot 16^2 \cdot 11^2 = 1\,424\,896$ and $n_2 = 11 \cdot 4^3 \cdot 56^2 = 2\,207\,744$ degrees of freedom. Thus the total number of degrees of freedom is reduced from $n_1 \cdot n_2 = 3.15 \cdot 10^{12}$ to $(n_1 + n_2) \cdot r + r^2 = 18\,163\,225$, which is a reduction by a factor of approximately $1.7 \cdot 10^5$.

We consider the following initial distribution

$$P(0, x) = \gamma \cdot \exp\left(-\frac{1}{2}(x - \mu)^T C^{-1}(x - \mu)\right),$$

with $C = 0.2$, $\mu = (40, 0, 0, 0, 0, 0, 0, 0, 0, 50, 0)$ and γ was determined by the condition that $\sum_{x \in \Omega^{\zeta, \eta}} P(0, x) = 1$. We performed the computations for the DLR approximation with the second-order integrator with 100 substeps and using a variable time step size. This time step size was adjusted according to the maximal reaction rate obtained by solving the rate equations deterministically (which is very cheap); the minimal time step size is $\tau = 1.0$. Due to the large system size, solving the full CME on the truncated state space was clearly not possible (we would need approximately 50 TB of main memory). For comparison we thus consider SSA simulations with *StochKit2*. The total run time of the DLR approximation and SSA computations is listed in table 5.

	run time [s]
DLR approx. ($r = 5$)	$1.3 \cdot 10^5$
SSA (10 000 runs)	84
SSA (100 000 runs)	129
SSA (1 000 000 runs)	358
SSA (10 000 000 runs)	2898

Table 5: Overview of the approximate run times in seconds for the DLR approximation and SSA for the BAX pore assembly system. The DLR approximation was computed with the second-order integrator using a variable time step size and 100 substeps. All computations were performed on a workstation with a 2.9 GHz Intel Core i5 Comet Lake (10400F) processor. The results of the DLR approximation were computed with six threads.

Figure 7 shows the partially evaluated probability distribution $P_S(x_1) = P(x_1, x_2 = 9, x_3 = 2, x_4 = 1, x_5 = 0, x_6 = 0, x_7 = 0, x_8 = 0, x_9 = 0, x_{10} = 50, x_{11} = 0)$ at time $t = 145$ computed with the DLR approximation using rank $r = 5$ and with SSA using 10 000, 100 000, 1 000 000 and 10 000 000 runs. The results of both methods are in good agreement, which demonstrates that in principle even such large problems can be solved with our implementation of the DLR approximation. Even though we use a

large number of samples, SSA has again problems to resolve the tail of the distribution. Although, we have no exact solution and thus can not confirm this with certainty, the tail of the dynamical low-rank approximation follows a power law that looks correct.

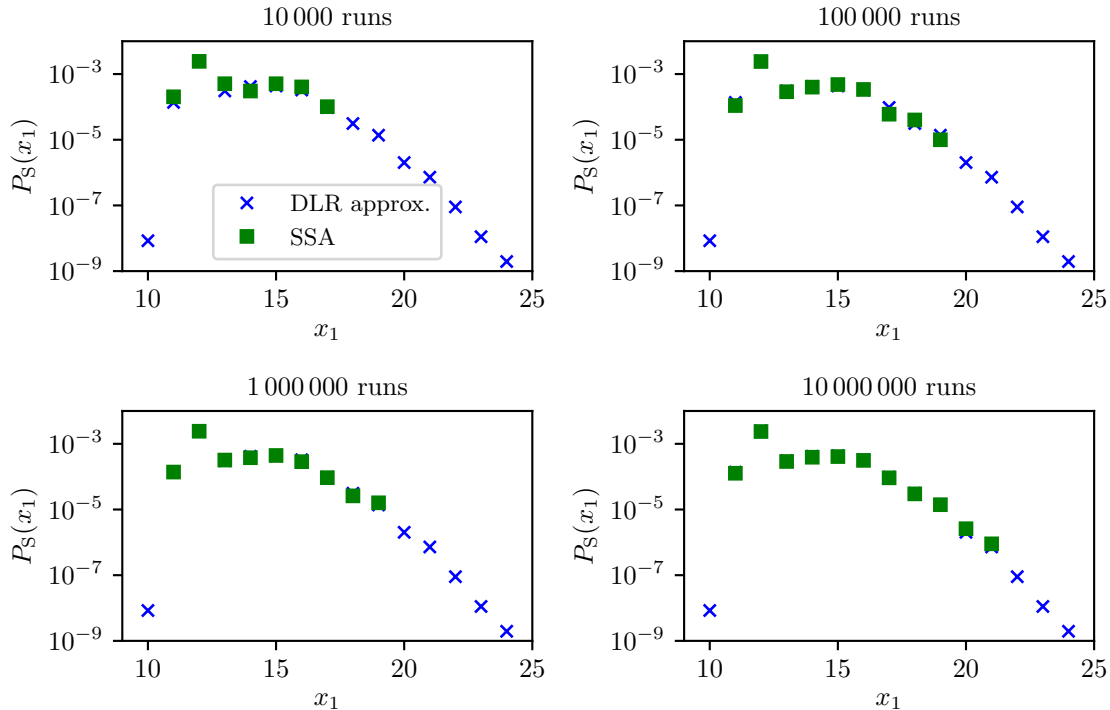


Figure 7: Partial evaluated probability distribution $P_S(x_1) = P(x_1, x_2 = 9, x_3 = 2, x_4 = 1, x_5 = 0, x_6 = 0, x_7 = 0, x_8 = 0, x_9 = 0, x_{10} = 50, x_{11} = 0)$ of the BAX pore assembly system at $t = 145$. The results were obtained with our implementation of the DLR approximation using rank $r = 5$ (red dots) and with SSA (green squares) using 10 000, 100 000, 1 000 000 and 10 000 000 runs. For the DLR approximation the second-order integrator with variable time step size and 100 substeps were used.

In figure 8 the partially evaluated two-dimensional probability distribution $P_S(x_1, x_2) = P(x_1, x_2, x_3 = 2, x_4 = 1, x_5 = 0, x_6 = 2, x_7 = 0, x_8 = 0, x_9 = 0, x_{10} = 50, x_{11} = 0)$ is shown for the same setup. For coloring a logarithmic mapping was employed; white areas indicate very small negative (and therefore unphysical) results for the DLR approximation and zero events in the case of SSA. Again, both methods yield similar results for large probability values, but it can be clearly seen that the DLR approximation captures areas of low probability which are not present in the SSA results.

Note that in terms of run time, SSA currently beats the DLR approximation for this large problem. However, when extending the DLR approach to a hierarchical scheme (where we divide the reaction network into more than two partitions) where subproblems have a similar size as the lambda phage problem, we expect that the run time would be comparable to the one for the lambda phage example with the additional benefit that the solutions are noise-free. We consider this the subject of future work.

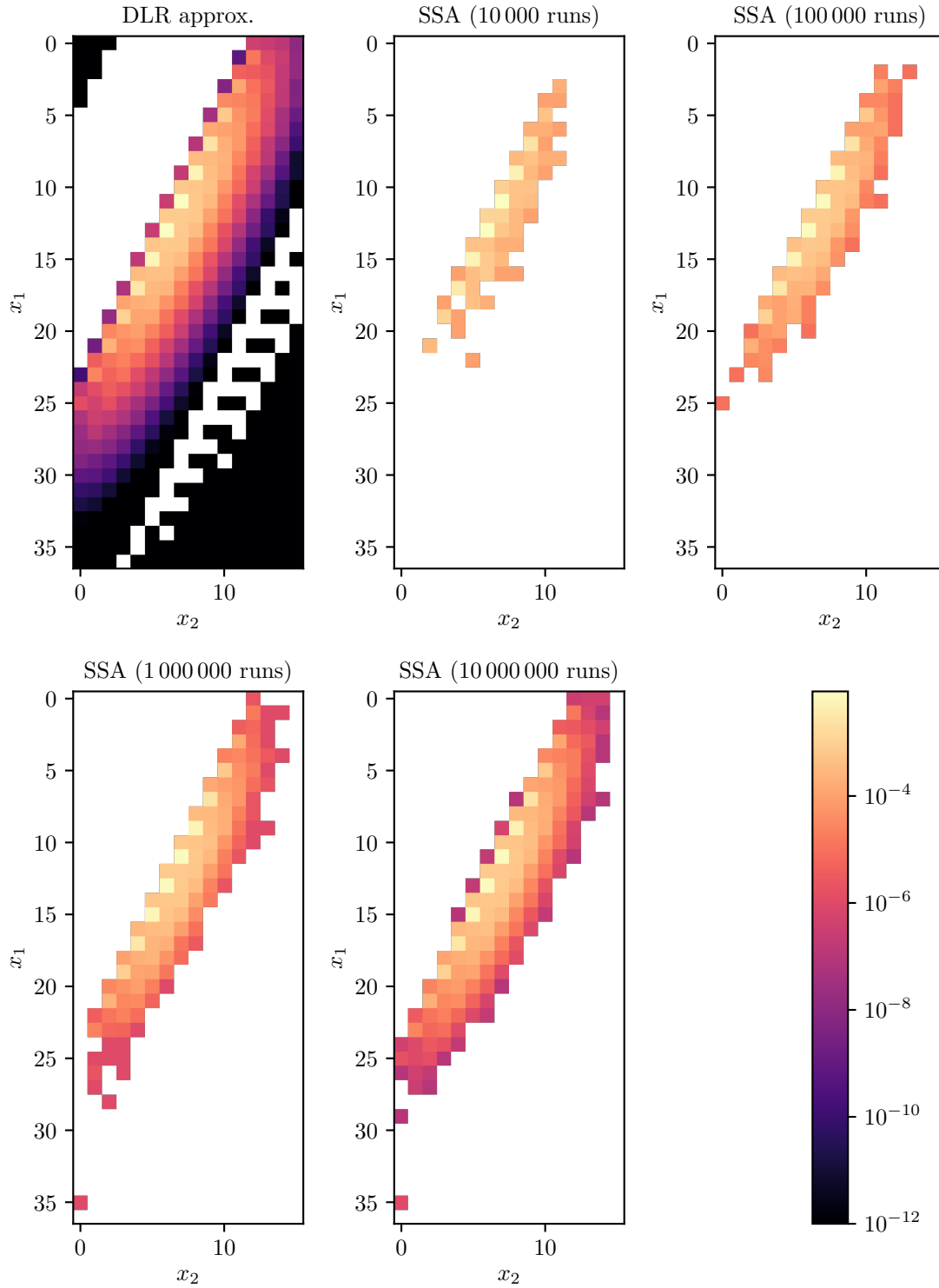


Figure 8: Partially evaluated two-dimensional probability distribution $P_S(x_1, x_2) = P(x_1, x_2, x_3 = 2, x_4 = 1, x_5 = 0, x_6 = 0, x_7 = 0, x_8 = 0, x_9 = 0, x_{10} = 50, x_{11} = 0)$ of the BAX pore assembly system at $t = 145$. The results were obtained with our implementation of the DLR approximation using rank $r = 5$ and with SSA using 10 000, 100 000, 1 000 000 and 10 000 000 runs. For the DLR approximation the second-order integrator with variable time step size and 100 substeps were used. Note that for coloring a logarithmic mapping was employed; white areas indicate very small negative (and therefore unphysical) results for the DLR approximation and zero events in the case of SSA.

6 Conclusion and outlook

The present work shows that using dynamical low-rank approximations can result in an algorithm that drastically reduces the memory and computational effort that is required in order to solve the chemical master equation. The proposed approach can even outperform SSA by a significant margin. It is further interesting to note that the DLR approach directly provides a low-storage approximation of the probability distribution function (which in SSA has to be reconstructed from the samples collected as a post-processing step).

The present work considers dividing the problem into two partitions. However, for large problems this is not sufficient in order to reduce the memory requirement and computational time to an acceptable level (and thus to outperform SSA). Thus, as future work, we will consider the techniques in [40, 19, 9, 8] in order to extend the proposed method to a hierarchical division into multiple partitions.

One significant advantage of the dynamical low-rank approach considered here is that it lends itself very well to implicit methods (compared to, e.g., a step-truncation low-rank approach as considered in [2, 4, 28, 33]). This is a significant advantage for solving the CME as reaction networks often include reactions with widely disparate time scales, thus making the resulting equations stiff. We note that this is also an issue for SSA (see, e.g., [29]).

References

- [1] J. G. Albeck, J. M. Burke, S. L. Spencer, D. A. Lauffenburger, and P. K. Sorger. Modeling a Snap-Action, Variable-Delay Switch Controlling Extrinsic Cell Death. *PLoS Biol.*, 12(6):2831–2852, 2008.
- [2] F. Allmann-Rahn, R. Grauer, and K. Kormann. A parallel low-rank solver for the six-dimensional Vlasov–Maxwell equations. *J. Comput. Phys.*, 469:111562, 2022.
- [3] A.-L. Barabási. Scale-Free Networks: A Decade and Beyond. *Science*, 325(5939):412–413, 2009.
- [4] X. Cai, W. Guo, and J.-M. Qiu. A high order conservative semi-Lagrangian discontinuous Galerkin method for two-dimensional transport simulations. *J. Sci. Comput.*, 73, 2017.
- [5] F. Cassini and L. Einkemmer. Efficient 6D Vlasov simulation using the dynamical low-rank framework *Ensign. Comput. Phys. Commun.*, 280, 2022.
- [6] G. Ceruti, J. Kusch, and C. Lubich. A rank-adaptive robust integrator for dynamical low-rank approximation. *BIT Numer. Math.*, 62:1149–1174, 2022.
- [7] G. Ceruti and C. Lubich. An unconventional robust integrator for dynamical low-rank approximation. *BIT Numer. Math.*, 62(1):23–44, 2022.
- [8] G. Ceruti, C. Lubich, and D. Sulz. Rank-adaptive time integration of tree tensor networks. *SIAM J. Numer. Anal.*, 61(1):194–222, 2023.
- [9] G. Ceruti, C. Lubich, and H. Walach. Time integration of tree tensor networks. *SIAM J. Numer. Anal.*, 59(1):289–313, 2021.
- [10] W. W. Chen, M. A. Niepel, and P. K. Sorger. Classic and contemporary approaches to modeling biochemical reactions. *Genes Dev.*, 24(17):1861–1875, 2010.
- [11] M. A. Clarke and J. Fisher. Executable cancer models: successes and challenges. *Nat. Rev. Cancer*, 20:343–354, 2020.
- [12] J. Coughlin and J. Hu. Efficient dynamical low-rank approximation for the Vlasov–Ampère–Fokker–Planck system. *J. Comput. Phys.*, 470:111590, 2022.
- [13] Z. Ding, L. Einkemmer, and Q. Li. Dynamical Low-Rank Integrator for the Linear Boltzmann Equation: Error Analysis in the Diffusion Limit. *SIAM J. Numer. Anal.*, 59(4), 2021.

- [14] L. Einkemmer. Accelerating the simulation of kinetic shear Alfvén waves with a dynamical low-rank approximation. *arXiv*, 2023.
- [15] L. Einkemmer, J. Hu, and J. Kusch. Asymptotic-preserving and energy stable dynamical low-rank approximation. *arXiv*, 2022.
- [16] L. Einkemmer, J. Hu, and Y. Wang. An asymptotic-preserving dynamical low-rank method for the multi-scale multi-dimensional linear transport equation. *J. Comput. Phys.*, 439(110353):110353, 2021.
- [17] L. Einkemmer, J. Hu, and L. Ying. An Efficient Dynamical Low-Rank Algorithm for the Boltzmann-BGK Equation Close to the Compressible Viscous Flow Regime. *SIAM J. Sci. Comput.*, 43(5):B1057–B1080, 2021.
- [18] L. Einkemmer and I. Joseph. A mass, momentum, and energy conservative dynamical low-rank scheme for the Vlasov equation. *J. Comput. Phys.*, 443:110495, 2021.
- [19] L. Einkemmer and C. Lubich. A Low-Rank Projector-Splitting Integrator for the Vlasov-Poisson Equation. *SIAM J. Sci. Comput.*, 40(5):B1330–B1360, 2018.
- [20] L. Einkemmer, A. Ostermann, and C. Piazzola. A low-rank projector-splitting integrator for the Vlasov–Maxwell equations with divergence correction. *J. Comput. Phys.*, 403:109063, 2020.
- [21] L. Einkemmer, A. Ostermann, and C. Scalone. A robust and conservative dynamical low-rank algorithm. *J. Comput. Phys.*, 484:112060, 2023.
- [22] C. Gardiner. *Handbook of Stochastic Methods*. Springer Berlin, Heidelberg, 2004.
- [23] T. S. Gardner, C. R. Cantor, and J. J. Collins. Construction of a genetic toggle switch in *Escherichia coli*. *Nature*, 403:339–342, 2000.
- [24] S. Gaudet, S. L. Spencer, W. W. Chen, and P. K. Sorger. Exploring the Contextual Sensitivity of Factors that Determine Cell-to-Cell Variability in Receptor-Mediated Apoptosis. *PLoS Comput. Biol.*, 4(8), 2012.
- [25] D. T. Gillespie. A general method for numerically simulating the stochastic time evolution of coupled chemical reactions. *J. Comp. Phys.*, 22(4):403–434, 1976.
- [26] D. T. Gillespie. A rigorous derivation of the chemical master equation. *Physica A*, 188(1):404–425, 1992.
- [27] R. Grima and S. Schnell. Modelling reaction kinetics inside cells. *Essays Biochem.*, 45:41–56, 2008.
- [28] W. Guo and J.-M. Qiu. A conservative low rank tensor method for the Vlasov dynamics. *arXiv*, 2022.
- [29] L. A. Harris and P. Clancy. A “partitioned leaping” approach for multiscale modeling of chemical reaction dynamics. *J. Chem. Phys.*, 125(14), 2006.
- [30] M. Hegland, C. Burden, L. Santoso, S. MacNamara, and H. Booth. A solver for the stochastic master equation applied to gene regulatory networks. *J. Comput. Appl. Math.*, 205:708–724, 2007.
- [31] T. Jahnke and W. Huisinga. A Dynamical Low-Rank Approach to the Chemical Master Equation. *Bull. Math. Biol.*, 70:2283–2302, 2008.
- [32] O. Koch and C. Lubich. Dynamical Low-Rank Approximation. *SIAM Journal on Matrix Analysis and Applications*, 29(2):434–454, 2007.
- [33] K. Kormann. A semi-Lagrangian Vlasov solver in tensor train format. *SIAM J. Sci. Comput.*, 37:613–632, 2015.
- [34] J. Kusch, L. Einkemmer, and G. Ceruti. On the Stability of Robust Dynamical Low-Rank Approximations for Hyperbolic Problems. *SIAM J. Sci. Comput.*, 45(1):A1–A24, 2023.
- [35] J. Kusch and P. Stammer. A robust collision source method for rank adaptive dynamical low-rank approximation in radiation therapy. *ESAIM: Math. Model. Numer. Anal.*, 57(2):865–891, 2023.

- [36] J. Kusch, B. Whewell, R. McClarren, and M. Frank. A low-rank power iteration scheme for neutron transport critically problems. *arXiv*, 2022.
- [37] C. F. Lopez, J. L. Muhlich, J. A. Bachman, and P. K. Sorger. Programming biological models in Python using PySB. *Mol. Syst. Biol.*, 9(1):646, 2013.
- [38] C. Lubich. *From quantum to classical molecular dynamics: reduced models and numerical analysis*. European Mathematical Society, 2008.
- [39] C. Lubich and I. V. Oseledets. A projector-splitting integrator for dynamical low-rank approximation. *BIT Numer. Math.*, 54(1):171–188, 2014.
- [40] C. Lubich, T. Rohwedder, R. Schneider, and B. Vandereycken. Dynamical approximation by hierarchical Tucker and tensor-train tensors. *SIAM J. Matrix Anal. Appl.*, 34(2):470–494, 2013.
- [41] H.-D. Meyer, F. Gatti, and G. A. Worth. *Multidimensional quantum dynamics*. John Wiley & Sons, 2009.
- [42] H.-D. Meyer, U. Manthe, and L. S. Cederbaum. The multi-configurational time-dependent Hartree approach. *Chem. Phys. Letters*, 165:73–78, 1990.
- [43] B. Munschy and M. Khammash. The finite state projection algorithm for the solution of the chemical master equation. *J. Chem. Phys.*, 124(4):044104, 2006.
- [44] M. Niepel, S. L. Spencer, and P. K. Sorger. Non-genetic cell-to-cell variability and the consequences for pharmacology. *Curr. Opin. Chem. Biol.*, 13(5-6):556–561, 2009.
- [45] P. Paszek, S. Ryan, L. Ashall, K. Sillitoe, C. V. Harper, D. G. Spiller, D. A. Rand, and M. R.H. White. Population robustness arising from cellular heterogeneity. *PNAS*, 107(25):11644–11649, 2010.
- [46] Z. Peng and R. McClarren. A high-order/low-order (HOLO) algorithm for preserving conservation in time-dependent low-rank transport calculations. *J. Comput. Phys.*, 447(110672), 2021.
- [47] Z. Peng, R. McClarren, and M. Frank. A low-rank method for two-dimensional time-dependent radiation transport calculations. *J. Comput. Phys.*, 421(109735), 2020.
- [48] M. Prugger, L. Einkemmer, and C. F. Lopez. A dynamical low-rank approach to solve the chemical master equation for biological reaction networks. *J. Comput. Phys.*, 489, 2023.
- [49] K. R. Sanft, S. Wu, M. Roh, J. Fu, R. K. Lim, and L. R. Petzold. StochKit2: software for discrete stochastic simulation of biochemical systems with events. *Bioinformatics*, 27(17):2457–2458, 2011.
- [50] M. K. Tonn, P. Thomas, M. Barahona, and D. A. Oyarzún. Stochastic modelling reveals mechanisms of metabolic heterogeneity. *Commun. Biol.*, 2(108), 2019.
- [51] A. Yachie-Kinoshita, K. Onishi, J. Ostblom, M. A. Langley, E. Posfai, J. Rossant, and P. W. Zandstra. Modeling signaling-dependent pluripotency with Boolean logic to predict cell fate transitions. *Mol. Syst. Biol.*, 14(1), 2018.
- [52] J. G. T. Zañudo, S. N. Steinway, and A. Réka. Discrete dynamic network modeling of oncogenic signaling: Mechanistic insights for personalized treatment of cancer. *Curr. Opin. Syst. Biol.*, 9:1–10, 2018.